International Journal of Rock Mechanics & Mining Sciences 134 (2020) 104461

Contents lists available at ScienceDirect

International Journal of Rock Mechanics and Mining Sciences

journal homepage: http://www.elsevier.com/locate/ijrmms

Permeability evolution and crack characteristics in granite under treatment at high temperature

Wen-Ling Tian [a,b], Sheng-Qi Yang [a,*], Derek Elsworth [b], Jian-Guo Wang [a], Xiao-Zhao Li [a]

[a] State Key Laboratory for Geomechanics and Deep Underground Engineering, School of Mechanics and Civil Engineering, China University of Mining and Technology, Xuzhou, 221116, PR China

[b] Department of Energy and Mineral Engineering, G3 Center, Pennsylvania State University, 231 Hosler Building, University Park, PA, USA

ARTICLE INFO

Keywords:
Granite
High temperature
Effective stress
Permeability
Microcrack characteristics

ABSTRACT

The evolution of permeability and microcrack characteristics of granite at high temperature has significant effect on the safe and stable operation of high-level nuclear waste disposal repositories. We measure the permeability, porosity and formation factors of granite specimens following thermal treatment including the use of NMR to certify observed response. The results indicate that the initial and residual permeability and porosity change little when $T \leq 300$ °C, but increase rapidly when 300 °C $\leq T \leq 600$ °C before entering a stable phase when 600 °C $\leq T \leq 750$ °C. At $T = 150$ °C microcrack apertures and radius only slight increase while microcrack density and fraction of connectedness all slight decrease, but net causing porosity, the peak strength and elastic modulus to increase. The strength and elastic modulus decrease exponentially with fractional connectivity of microcrack while the initial compressibility of microcracks scale linearly with initial aperture. The formation factor for the granite increases near-linearly with effective stress with the rate of increase generally decreasing with increasing temperature. Thermal conductivity first increases rapidly before remaining constant with increasing effective stress. With increasing temperature, the thermal conductivity decreases and becomes more sensitive to the effective stress.

1. Introduction

Granite is potentially an excellent medium for high-level nuclear waste (HLW) disposal, exhibiting low native permeability and high integrity.[1–4] Beishan granite has been selected as a candidate for HLW geological disposal in China – with such a low native permeability. However, the in situ permeability may increase due to both excavation and the generation of thermally-induced crack (The temperature is high as 1200 °C in nuclear self-storage[5]). These factor increase the risk for radionuclides to access the biosphere and human environment.

Permeability of tight fractured rocks is particularly sensitive to effective stress - thus it is crucial to investigate the permeability behavior around any HLW repository.[2] Power law[6] and exponential relations[7] between permeability and effective stress have been applied as representative of permeability data for a large number of samples. However, gas slippages effect play a positive role in improving permeability, of which the Klinkenberg permeability shows a positive linear relationship with the total permeability.[8] Using both non-adsorbing and absorbing gases, the causes of permeability decreases for adsorbing gases has been defined.[9] Under unloading, significant hysteresis was apparent that may be described via models accommodating frictional sliding inside the rock.[10]

High temperatures may induce microcrack formation and propagation and result in an increase in permeability. However, very high temperatures impart ductility to the minerals and may drive a reduction in permeability.[4,11] Changes in permeability result from the competition between these opposing effects. When $T \leq 400$ °C, permeability may decrease with increasing temperature,[12] where the dissolution of quartz and feldspar and redeposition of these mineral within cracks at lower temperature is known to be a major cause in the reduction of permeability.[13] However, temperatures elevated to only moderate levels can also enhance permeability due to the heterogeneity in thermal expansion of the constituent minerals. Conversely, the activation of plastic processes at higher temperature causes the collapse of void spaces and reduction of permeability capacity.[14] The evolution of permeability with temperature is also affected by the effective stress where a temperature increases leads first to a permeability decrease and then to its increase at low effective pressure, although inversions may appear on all the temperature trends of the samples collected from great depth at higher

* Corresponding author.
E-mail address: yangsqi@hotmail.com (S.-Q. Yang).

https://doi.org/10.1016/j.ijrmms.2020.104461
Received 14 January 2020; Received in revised form 5 August 2020; Accepted 7 August 2020

List of symbols

T	Temperature
HLW	High-level nuclear waste
XRD	X-ray diffraction
K_g	Gas permeability
K_l	Liquid permeability
P_{av}	Pore pressure
b	Klinkenberg constant
k	Permeability
Q	Downstream gas flow rate
A	Cross-sectional area of the specimen
H	Length of the specimen
k_0	Initial permeability
k_∞	Residual permeability
c_0	Initial compressibility
α	Decline rate of crack compressibility with effective stress
R^2	Correlation coefficient
V_w	Water volume
V_0	Rock specimen volume
F	Formation factor
C_w	Electric conductivity of a solution
C_0	Electric conductivity of saturated rock
ϕ	Porosity
n_0	Number of cracks per unit volume
c	Microcrack radius
w	Micro-crack half-aperture
A	Aspect ratio
θ	Hydrodynamics of flow through a system of cracks of varying thickness
f	Fraction of the cracks that belong to an infinite network
l	Spacing between two cracks
p	Probability of two cracks intersecting
V_e	Excluded volume for two cracks
ds	Increment of crack displacement
$d\sigma$	Increment of effective stress
ϕ_0	Initial porosity
K	Thermal conductivity
K_s	Thermal conductivity of solid grains
K_g	Thermal conductivity of air
σ_s	The peak strength
E_s	Elastic modulus
NMR	Nuclear magnetic resonance
r	Pore radius
T_2	Transverse relaxation time
ρ	Transverse surface relaxation strength of rocks
S	Pore surface area
V	Pore volume
F_s	Geometry factor

effective pressure.[15] The permeability of a single fracture in granite is also affected by stress and temperature with dissolution effects and fracture closure being implicated even at low temperatures when $T = 90\ ^\circ C$[16] similar to constraint due to thermal expansion increasing normal stress in the fracture.[17] The evolution of permeability with temperature may be indexed relative to the number of AE events[18,19] and changes in quality and wave velocity are capable of linking directly to permeability.[20]

However, the permeability and microcrack characteristics of granite following thermal treatment have not been systematically investigated. In this work, we investigate the evolution of microcrack aperture, density and radius with temperature and effective stress to link permeability evolution under different effective stresses and for granites of differing porosity and formation factor following thermal treatment.

2. Experimental methodology

2.1. Granite material

The granite used in this work was collected from the city of Rizhao in Shandong province, China. According to the results of X-ray diffraction (XRD), the minerals in the granite are quartz (11.12%), feldspar (59.85%), biotite (21.56%), amphibole (6%), chlorite (1.01%) and dolomite (0.46%). This granite has a crystalline and blocky structure with a connected porosity of 0.67%.[1] The average density of the tested granite at room temperature is ~2594 kg/m^3 with a P-wave velocity of ~4200 m/s. All cylindrical specimens were cored from the same block of material to an actual diameter of 50 mm and approximately 100 mm in length. Before beginning the permeability tests, the granite specimens were first placed in a furnace and heated at a rate of 5 °C/min to minimize thermal shock. Once reaching their predetermined temperature, the samples retained at that temperature for 2 h to ensure the uniformity in temperature across the specimen. For permeability tests, the target treatment temperatures were set as 150, 300, 450, 600 and 750 °C. Finally, the heated specimens were left in the furnace to cool down to room temperature.

2.2. Permeability testing system and procedure

It is difficult to measure the coefficient of permeability from steady-state liquid flow tests in tight rocks as the measuring time is typically long, ranging from weeks to months for the measurement of a single specimen.[21] Based on Klinkenberg,[22] gas (K_g) and liquid (K_l) permeability are related as $K_g = K_l(1 + b/P_{av})$, where P_{av} is pore pressure, and b is the Klinkenberg constant. If the pore pressure is retained constant (4 MPa) then there is a linear relationship between K_l and K_g. Thus, nitrogen (N_2) was used to measure the permeability of granite following thermal treatment under different effective stresses.

The gas permeability test system (Fig. 1) includes a pressure intensifier and core holder capable of applying hydrostatic stress and controlling and acquiring data from the experiment. A jacketed cylindrical specimen (14) is confined within the high pressure vessel (13). Confining pressure is provided by a constant flow pump (15), and held by pressure control (23). It should be noted that the maximum triaxial pressure of the test system is 60 MPa, which is smaller than the compressive strength of the granite tested in this experiment. The gas pressure intensifier consists of a gas tank (3), gas pipes, and valves (6, 7, 10, 11) tighter with a gas pump (1) capable of increasing the gas pressure effectively from 0 to 3 MPa to 0–40 MPa. The gas pressure sensors operate on three different scales (20, 21, 22) to improve the accuracy of the measurements.

The permeability of the granite specimens can be calculated according to Darcy's law under steady-state flow conditions[23] as:

$$k = \frac{2QP_2\mu H}{(P_1^2 - P_2^2)A} \quad (1)$$

where Q is the downstream gas flow rate, A and H are the cross-sectional area and the length of the specimen, respectively, P_1 and P_2 are the pressure on the upstream side and standard atmospheric pressure at room temperature on the downstream and μ is the viscosity of the fluid ($\mu \approx 1.8 \times 10^{-5}$ Pa s for pure nitrogen at room temperature under the applied pore pressure).

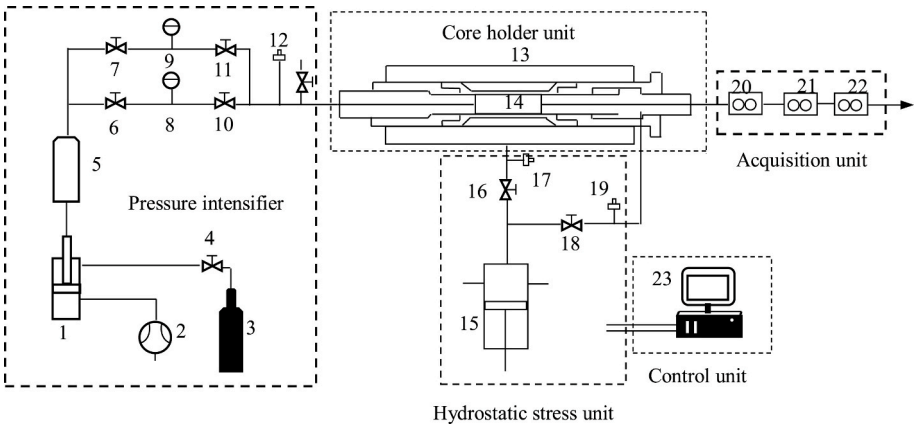

Fig. 1. Schematic representation of the automated permeability measurement system.

3. Experimental results

Fig. 2 shows the evolution of permeability of the granite specimens following thermal treatment with effective stress. Permeability decreases exponentially with increasing effective stress, regardless of the treatment temperature. With treatment temperature increasing from 25 °C to 300 °C, the permeability slowly increases with temperature. However, when $T = 450$ and 600 °C, the permeability increases markedly. When $T = 750$ °C, increasing temperature has only a slight impact on permeability.

Assuming that the compressibility of the pore or a crack decreases exponentially with effective stress, the average bulk compressibility of the pore can be represented as $\overline{c_p} = \frac{1}{\sigma-\sigma_0}\int_{\sigma_0}^{\sigma} c_0 e^{-\alpha(\sigma-\sigma_0)}d\sigma = \frac{c_0}{\alpha\Delta\sigma}(1 - e^{-\alpha\Delta\sigma})$. Where McKee[9] derived a theoretical permeability model as:

$$k = k_0 e^{-3\frac{c_0}{\alpha}(1-e^{-\alpha\Delta\sigma})} \quad (2)$$

where k_0 and c_0 are initial permeability and compressibility, α is the decline rate of crack compressibility with effective stress.

Fig. 3 presents a comparison between theoretical and experimental results when $T = 150$ °C. The theoretical curve, evaluated from Eq. (2) agrees satisfactorily with the experimental results. The correlation coefficient ranges from 0.960 ($T = 750$ °C) to 0.999 ($T = 600$ °C), suggesting as strong correlation with Eq. (2) linking the evolution of permeability with effective stress, regardless of the treatment temperature. With increasing effective stress, the permeability of the heat-treated granite specimens first decreases rapidly then stabilizes.

From Fig. 3, the evolution of permeability with effective stress may be fit to Eq. (2), enabling initial (k_0) and residual (k_∞) permeability to be obtained. Fig. 4 illustrates the variation of initial and residual permeability with temperature. Initial and residual permeabilities have a similar trend with increasing temperature. The initial and residual permeabilities first slightly increase when temperature is ≤ 300 °C. In the range 25 °C ≤ T ≤ 100 °C, the absorbed water first evaporates and then at 100 °C ≤ T ≤ 300 °C the bound water escapes (Sun et al., 2015).

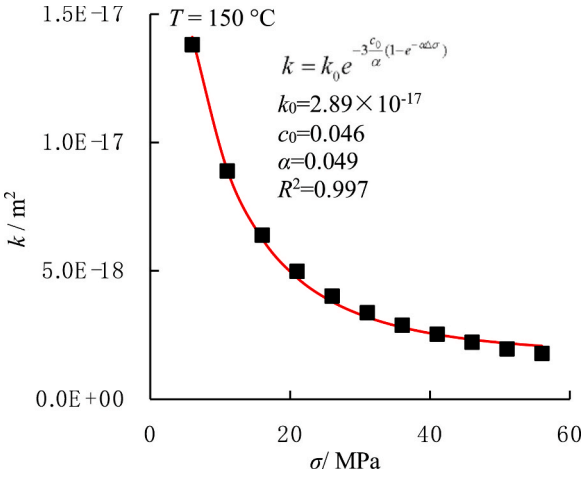

Fig. 3. Match of permeability data to model for granite specimens following thermal treatment.

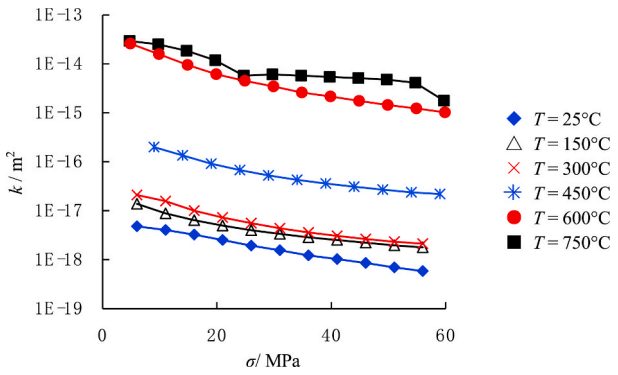

Fig. 2. Variation of permeability of granite with effective stress following thermal treatment.

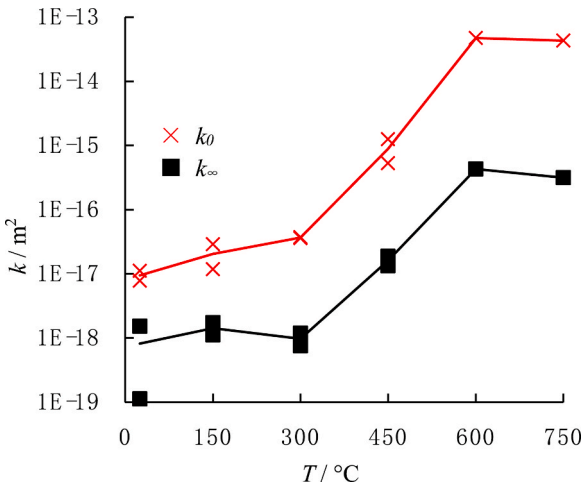

Fig. 4. Variation of initial and residual permeability with temperature.

The loss of the absorbed water and bound water may lead to an increased gas permeability. However, the initial and residual permeabilities increase quickly when the temperature rises from 300 °C to 600 °C, but then remain near constant when the temperature increases to 750 °C. High temperatures have a significant effect on initial and residual permeabilities of granite with increases of ~3–4 orders-of-magnitude when temperature increases from 25 °C to 750 °C.

Mercury injection porosimetry can be used to measure the porosity of the granite. However, the granite develops macro-cracks after the application of high temperatures and mercury injection porosimetry only measures the local porosity of the granite specimens. Therefore, the water saturation method was used to measure the porosity of the granite following thermal treatment. First the mass was obtained before saturation, and then remeasured after saturated by a salt solution. Finally, the porosity (ϕ) can be calculated as:

$$\phi = \frac{V_w}{V_0} = \frac{m_w}{V_0 \rho_w} \tag{3}$$

where V_w and V_0 are water volume and rock specimen volume after saturation, and m_w and ρ_w are water mass and density.

From Fig. 5 it is apparent that the porosity of the granite remains near constant with temperature increasing in the range 25 °C–300 °C, with a slight rise as temperature increases to 450 °C. However, porosity rapidly increases with temperature increases from 450 °C to 600 °C, due to thermal cracks induced by the phase transformation of quartz at $T =$ 573 °C. Finally, porosity slightly increases when temperature increases from 600 °C to 750 °C.

The relationship between water saturation and rock specific electrical resistance is described by the Archie equation.[24] In this model, the ratio between electric conductivity of a solution (C_w) and that of the saturated rock (C_0) is defined as a formation factor and it has reciprocal relationship with porosity:

$$F = \frac{C_w}{C_0} = 4 f^{-1} \phi^{-1} \tag{4}$$

The electric conductivity of saturated rock can be obtained from a digital electric bridge where the electric conductivity of the salt solution is 850 μs/cm and enabling the transformation of the formation factor of the granite following thermal treatment to be obtained. As show in Fig. 6, the formation factor first slightly decreases as temperature is increased to 150 °C, then rapidly decreases as the temperature increases from 150 °C to 600 °C before finally remaining constant as temperature increases to 750 °C.

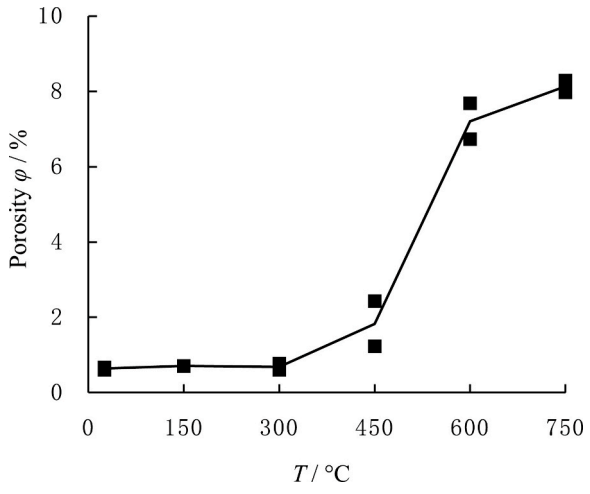

Fig. 5. Variation of porosity with temperature.

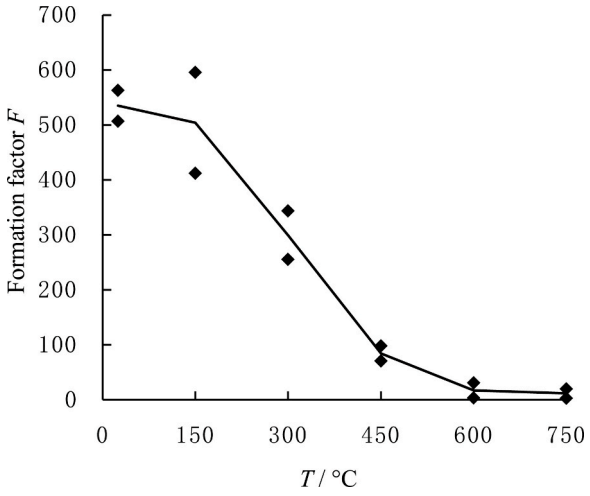

Fig. 6. Variation of granite formation factor with temperature.

4. Microcrack characteristics of granite following thermal treatment

Assuming that microcracks are distributed isotropically within the rock, we may use the relationship between permeability and microcrack characteristic as constructed by Dienes[25] as:

$$k = \frac{4\pi}{15} A^3 n_0 \overline{c^5} \theta f \tag{5}$$

where n_0 is number of cracks per unit volume (crack density), c is the microcrack radius, $A = w/c$ is the aspect ratio, and θ is the hydrodynamics of flow through a system of cracks of varying thickness.

For more uniform crack radius, then $\overline{c^5}$ can be replaced by $\overline{c}^5$. Then $n_0 = 1/\bar{\imath}^3$, where $\bar{\imath}$ is average spacing between two cracks. Thus, Eq. (5) can be simplified as:

$$k = \frac{4\pi}{15} f \frac{\overline{w}^3 \overline{c}^2}{\bar{\imath}^3} \tag{6}$$

The relationship between porosity and microcrack characteristic can be expressed as[26]:

$$\phi = 2\pi \frac{\overline{c}^2 \overline{w}}{\bar{\imath}^3} \tag{7}$$

Combined with Eqs. (6) and (7), the relationship between permeability and porosity can be expressed as:

$$k = \frac{2}{15} f \overline{w}^2 \phi \tag{8}$$

Combining with Eqs. (4) and (8), the microcrack half-aperture can be expressed as:

$$\overline{w} = 0.25 (30 k F)^{0.5} \tag{9}$$

In Eq. (9), k and F are initial permeability and formation factor, and the average microcrack half-aperture of the rock mass can be obtained. As depicted in Fig. 7, the average microcrack half-aperture first slightly rises when the temperature increases to 150 °C, and remains constant when the temperature increases to 300 °C - similar to the initial permeability. However, the average microcrack half-aperture rapidly increases when temperature increases from 300 °C to 600 °C before decreasing slightly when temperature rises to 750 °C.

Assuming that the center of the cracks are randomly distributed in the rock, the relationship between f and the probability of two cracks intersecting (p) can be expressed as[27]:

$$f = 54 (p - p_c)^2 \tag{10}$$

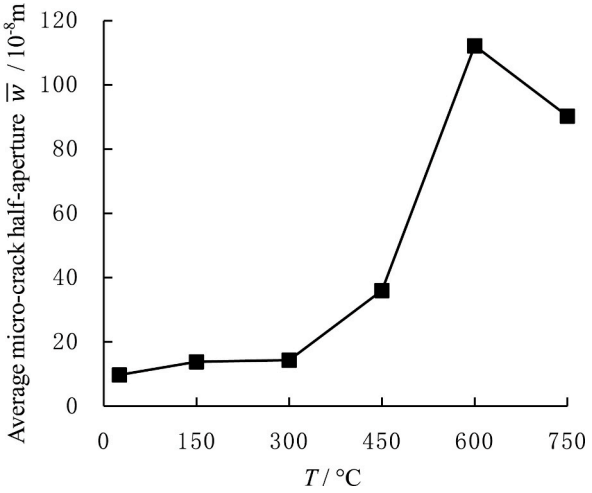

Fig. 7. Variation of average crack half-aperture with temperature.

where p_c is threshold probability. In this, each cracks has z neighbors, then $p_c = 1/(z\text{-}1)$. Assuming $z = 4$, then $p_c = 1/3$[25]. Below p_c, $f = 0$, and above p_c, f increases to 1.

Given the excluded volume for two cracks: $V_e = \pi^2\bar{c}^3$, the probability p is:

$$p = \frac{\pi^2}{4}\frac{\bar{c}^3}{\bar{l}^3} \tag{11}$$

Combined with Eqs. (7), (9)–(11), the average crack radius ($\bar{c}$) and average spacing between two cracks ($\bar{l}$) can be defined as:

$$\bar{c} = 2(\pi\phi)^{-1}(30kF)^{0.5}\left\{\frac{1}{3} + \left[2\,/\,(27F\phi)^{0.5}\right]\right\} \tag{12}$$

$$\bar{l} = \left(\frac{\pi^2}{4}\right)^{1/3}\bar{c}\left\{1/3 + \left[2/(27F\phi)^{0.5}\right]\right\}^{-1/3} \tag{13}$$

Using Eq. (12), enables the average microcrack radius of the heat-treated granite to be obtained. As shown in Fig. 8a, the average microcrack radius first rises when temperature increases to 450 °C, and then decreases when temperature increases to 600 °C and 750 °C. The average spacing between two cracks can be evaluated from Eq. (13), demonstrating a similar trend with average microcrack radius, as shown in Fig. 8b. Crack density can be obtained from $\overline{n_0} = 1/\bar{l}^3$, as depicted in Fig. 8c, defining crack density slightly decreases from 6.35×10^{19} m^{-3} to 2.52×10^{19} m^{-3} when $T \leq 450$ °C, and before increasing rapidly to 28.94×10^{19} m^{-3}.

Using Eq. (8), the fraction of connectedness of the microcracks can be obtained. As shown in Fig. 8d, the fraction of connectedness of the microcracks first decreases slightly at $T = 150$ °C, before increasing when temperature increases from 150 °C to 450 °C. However, the fraction of connectedness increases markedly when temperature increases from 450 °C to 600 °C before increases only slightly when $T =$ 750 °C. When $T = 600$ °C and 750 °C, more macrocracks are observed in the granite specimens with increasing crack density and fraction of connectedness.

The fraction of connectedness has the opposite trend with the uniaxial compressive strength, damage threshold strength and elastic modulus. Fig. 9 illustrates the relationship between fraction of connectedness and the peak strength, damage threshold strength (damage threshold strength correspond to the onset of dilatancy under loading process) and elastic modulus. The strength and elastic modulus decrease nonlinearly with increasing connectivity. The exponential form $y = ae^{bx}$ is used to fit the relationship between strength, elastic modulus and fraction of connectivity. The assumed function agree satisfactorily with the experimental results, and the correlation coefficients (R^2) are 0.97, 0.98 and 0.98 for the peak strength, damage threshold and elastic modulus, respectively.

Assuming that average microcrack radius, spacing and fraction of

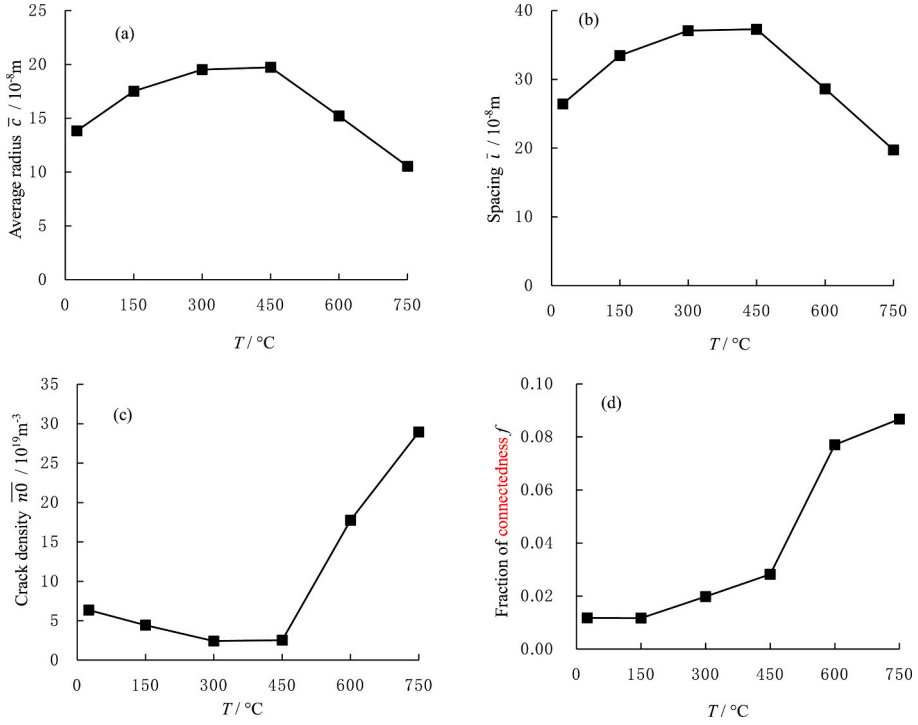

Fig. 8. Variation of average cracks radius, spacing, number of cracks per unit volume and fraction of connectedness with temperature: (a) Average radius c, (b) Spacing ι, (c) Crack density $\overline{n_0}$, (d) Fraction of connectedness f.

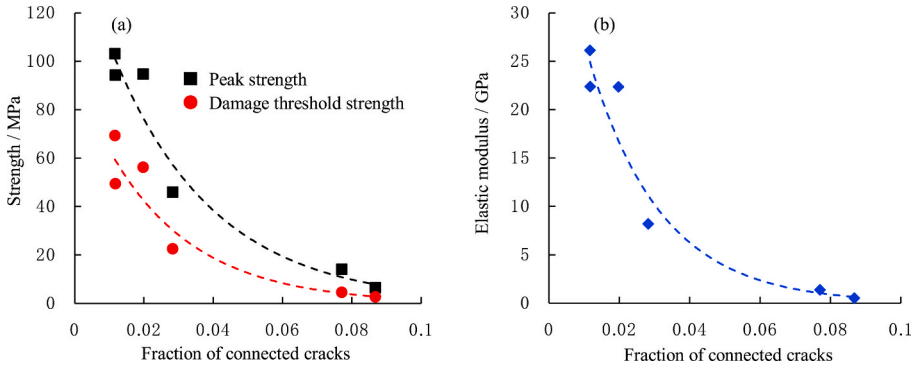

Fig. 9. Strength and elastic modulus of granite following thermal treatment with variation of fraction of connected cracks: (a) strength, (b) elastic modulus.

connectedness remaining constant with increasing effective stress, the evolution of average microcrack half-aperture can be obtained from Eq. (6). As shown in Fig. 10, average microcrack half-aperture decreases nonlinearly with increasing effective stress. The average microcrack half-aperture generally increases with increasing temperature, except for $T = 750$ °C.

As assumed in Eq. (2), compressibility of the microcrack decreases exponentially with effective stress:

$$c = c_0 e^{-\alpha(\sigma-\sigma_0)} \tag{14}$$

Assuming that effective stress only has an effect on fracture aperture, then c can be expressed as:

$$c = \frac{ds}{d\sigma} \tag{15}$$

where ds and $d\sigma$ are increment of crack displacement and effective stress.

Combining this with Eqs. (14) and (15), then ds can be expressed as:

$$ds = c_0 e^{-\alpha(\sigma-\sigma_0)} d\sigma \tag{16}$$

Assuming that the displacement of the crack is zero when no increment of effective stress is applied, then, Eq. (16) can be expressed as:

$$s = -\frac{c_0}{\alpha}(e^{-\alpha\sigma} - 1) \tag{17}$$

where $s = 2(w_0\text{-}w)$, w_0 is initial microcrack half-aperture, and w is the half-aperture of microcrack under effective stress σ. Therefore, Eq. (17) can be expressed as:

$$w = w_0 + \frac{c_0}{2\alpha}(e^{-\alpha\sigma} - 1) \tag{18}$$

Fig. 10 also shows a comparison between theoretical curves evaluated from Eq. (18) and the experimental results. The theoretical curves agree satisfactorily with the experimental results, and the correlation coefficient is in the range 0.968 ($T = 750$ °C) to 0.999 ($T = 450$ °C).

The evolution of average microcrack half-aperture with effective stress may be fit to Eq. (18), enabling the initial microcrack half-aperture, crack compressibility and their decline rates with heat-treatment to be obtained. As shown in Fig. 11a, the initial microcrack half-aperture first slightly increases as the temperature rises to 300 °C, and then increases markedly when temperature increases from 300 °C to 600 °C before decreasing only slightly when $T = 750$ °C.

The variation of microcrack compressibility is presented in Fig. 11b. As expected, microcrack compressibility has a similar trend to that of average microcrack half-aperture. The relationship between initial microcrack half-aperture and crack compressibility is shown in Fig. 11c. Microcrack compressibility increases near-linearly with increasing initial microcrack half aperture. Fig. 11d illustrates the variation in the decline rate of crack compressibility with temperature. The decline rate first increases when temperature increases to 150 °C and then remains near constant with increasing temperature.

5. Macro-characteristics following thermal treatment

After obtaining the evolution of microcrack half-aperture with effective stress, the evolution of porosity with effective stress may also be evaluated from Eq. (7). As shown in Fig. 12, the porosity of granite also decreases nonlinearly with increasing effective stress, regardless of the treatment temperature. However, porosity increases with increasing temperature at the same effective stress (except for $T = 300$ °C). Considering the residual porosity (ϕ_r), the relationship between porosity and effective stress may be defined as[28] (based on mass of experiments),

$$\phi = \phi_r + (\phi_0 - \phi_r) e^{\beta(\sigma-\sigma_0)} \tag{19}$$

Where ϕ_0 is initial porosity, and β is a material constant of the rock.

From Fig. 12, the theoretical curves obtained from Eq. (19) agree satisfactorily with the experimental results, and the correlation coefficient is in the range 0.936 ($T = 750$ °C) to 0.999 ($T = 450$ °C). This

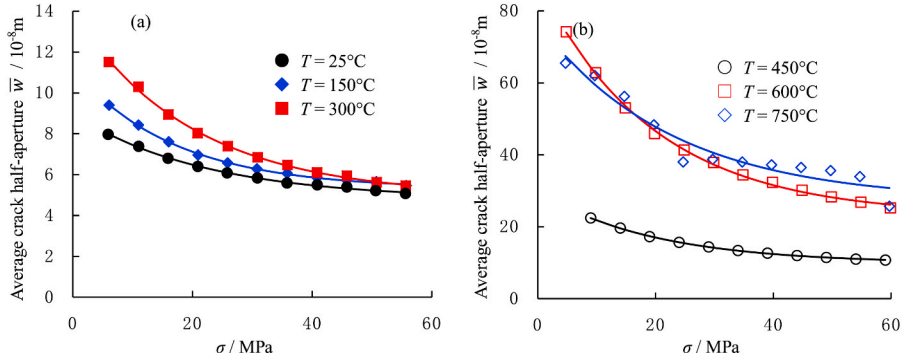

Fig. 10. Evolution of average crack half-aperture following thermal treatment with effective stress: (a) $T \leq 300$ °C, (b) $T \geq 450$ °C.

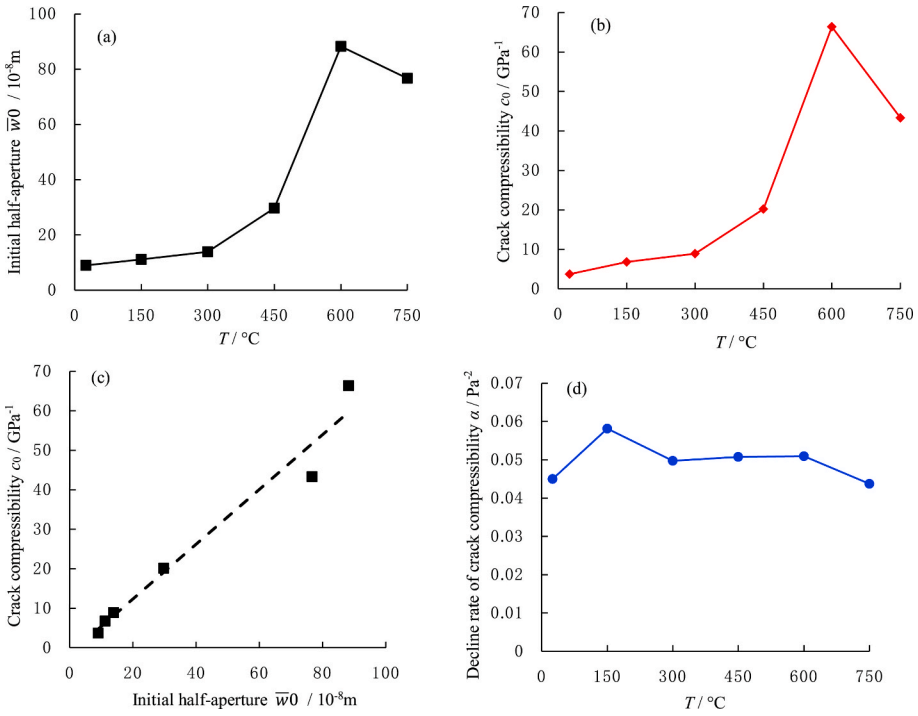

Fig. 11. Initial half-aperture, initial crack compressibility and the decline rate of heat-treated granite with effective stress: (a) w0, (b) c_0, (c) Relationship between w0 and c_0, (d) α.center.

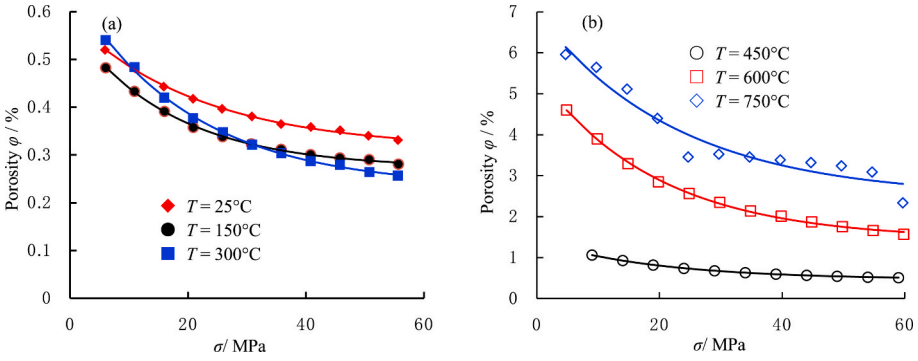

Fig. 12. Evolution of porosity of granite following thermal treatment with effective stress regressed by an improved exponential equation: (a) $T \leq 300$ °C, (b) $T \geq 450$ °C.

suggests that the porosity of granite obtained from Eq. (7) under changing effective stress has a similar trend with that obtained from prior investigations.

The residual porosity and material constant of granite following thermal treatment can be obtained from Eq. (19). As illustrated in Fig. 13a, the residual porosity first remains near constant when $T \leq 300$ °C, and then rises slightly as temperature increases from 300 °C to 450 °C. However, the residual porosity of the granite increases rapidly

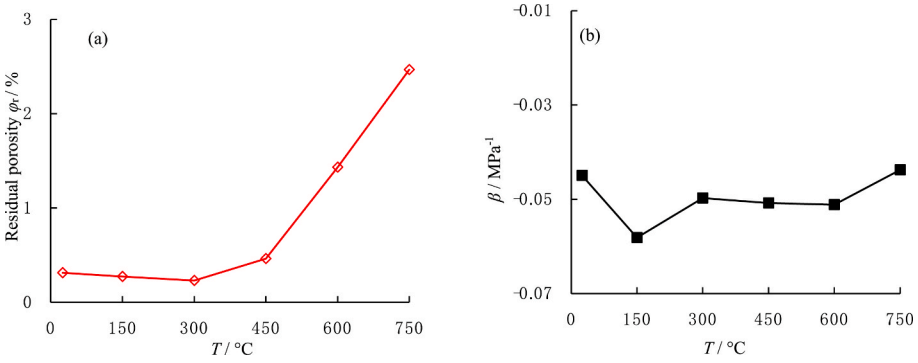

Fig. 13. Variation of residual porosity and β with temperature: (a) ϕ_r, (b) β.

when temperature increases from 450 °C to 750 °C. Compared with the initial porosity of the granite obtained from the experiments, as shown in Fig. 5, the initial and residual porosity shows a similar trend with increasing temperature, except at $T = 750$ °C. The material constant for granite sharply decreases with an increase in temperature to 150 °C and then increases when the temperature increases to 300 °C. After this, the material constant is in the range from -0.0508 MPa^{-1} to -0.0437 MPa^{-1}.

Using Eq. (9), the formation factor of the heat-treated granite under variable effective stress can also be obtained. As shown in Fig. 14, the formation factor increases near-linearly with increasing effective stress. With increasing temperature, the rate of increase and magnitude of the formation factor generally decrease.

Thermal conductivity is one of the most important parameters in the design of HLW repositories, due to its direct effect on the evaluation of the necessary repository volume and the optimization of the repository layout.[29,30] It has been confirmed that the thermal conductivity measured in-situ is typically higher than laboratory measurement, due to neglecting the impact of in-situ stress in the laboratory.[31,32] Consequently, there are few measurements of thermal conductivity of granite under effective stress. The relationship between thermal conductivity (K) and porosity of saturated sediments has been defined and, with the thermal conductivity of water replaced by air, the relationship between thermal conductivity and porosity of dry rock can be expressed as:

$$K = K_s \left[\frac{K_g}{K_s}\right]^{a\phi} \tag{20}$$

where K_s and K_g (0.025 W/mK) are thermal conductivity of solid grains and air, where a is a material constant of the rock.

The thermal conductivity and porosity of granite following thermal treatment can be measured experimentally, and constants for K_s (2.53 W/mK) and a (2.1) can be evaluated from Eq. (20). We have not considered the effect of thermal treatment on K_s, but thermal conductivity of the granite specimens following thermal treatment may be fit by Eq. (20). As depicted in Fig. 15, the thermal conductivity evaluated from Eq. (20) agrees satisfactorily with that obtained by experiment.

Therefore, the relationship between thermal conductivity and effective stress can be constructed, based on Eqs. (19) and (20):

$$K = K_s \left[\frac{K_g}{K_s}\right]^{a(\phi_r+(\phi_0-\phi_r))e^{\beta(\sigma-\sigma_0)}} \tag{21}$$

This enables thermal conductivity of the heat-treated granite under effective stress to be obtained. As shown in Fig. 16, thermal conductivity of the granite first increases rapidly before becoming constant with increasing effective stress, regardless of the treatment temperature. This trend is similar to that obtained by Görgülü et al.[33] and Zhao et al.[30] under uniaxial compression, and that obtained by Demirci et al.[34] under

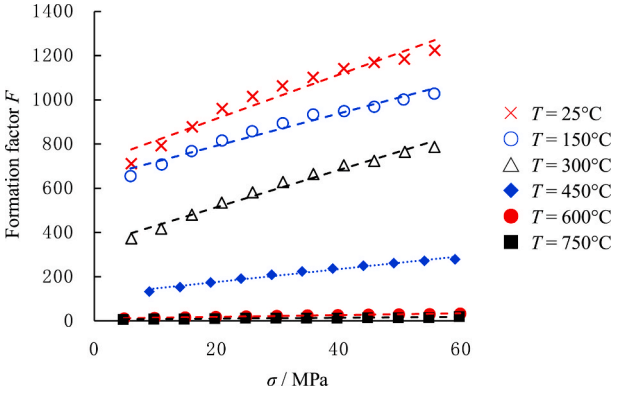

Fig. 14. Evolution of formation factor following thermal treatment with effective stress.

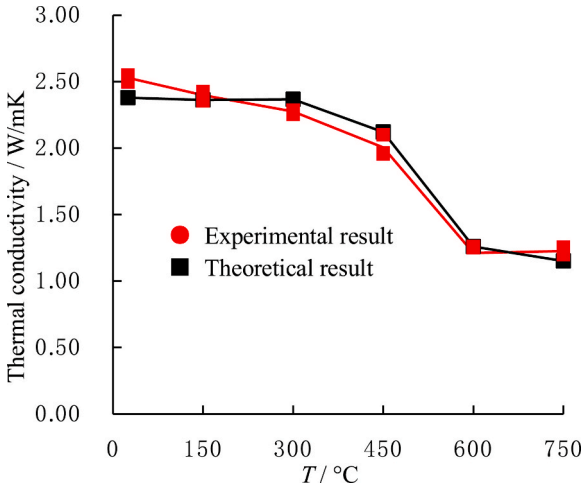

Fig. 15. Comparison between theoretical and measured thermal conductivities.

triaxial compression. When $T \leq 300$ °C, temperature has only a slight impact on the thermal treatment. However, when $T = 450$ °C, thermal conductivity decreases markedly under the same effective stress compared with that at $T \leq 300$ °C, and the nonlinear response is clear. When $T \geq 600$ °C, thermal conductivity continuously decreases with increasing temperature, and the nonlinear response is clear.

6. Discussion

Fig. 17 illustrates the variation of the peak strength (σ_s) and elastic modulus (E_S) of granite specimens with temperature. The peak strength and elastic modulus both first increase when temperature increases to 150 °C. As previously observed using SEM,[35] some initial microcracks and pores close, as induced by thermal expansion of the mineral grains, strengthening and increasing the integrity of the micro structure of the granite. This explanation accords with our observation that the crack density decreases when temperature increases to 150 °C, as shown in Fig. 8c. However, SEM is only able to scan a local portion of the specimen and cannot represent the global and aggregate interior characteristics of the overall specimen. Also it cannot explain the phenomenon that the permeability increases when temperature increases to 150 °C. From Figs. 7 and 8a, the average microcrack half-aperture and radius increases when $T = 150$ °C. From the above analysis, it can be concluded that some microcrack closure is induced by thermal treatment, this results in a decrease in crack density, and an increase in the peak strength and elastic modulus when $T = 150$ °C. However, thermal treatment also opens and propagates some microcracks, leading to an increase in the microcrack half-aperture and radius and a consequent permeability increases when $T = 150$ °C.

In other hand, heating lead to dehydration of granite. When 25 °C $\leq T \leq$ 100 °C, the absorbed water would be lost, and the bounded water and crystal water escape when 100 °C $\leq T \leq$ 300 °C.[36] Due to water lost, the friction between grains increases,[37,38] and the peak strength and elastic modulus of granite specimens rises when $T = 150$ °C, as shown in Fig. 17. The water lost also increases the aperture of micro-crack, which lead to the increase of permeability when $T = 150$ °C.

Nuclear magnetic resonance (NMR) provides a fast, convenient and non-contacted method for characterizing complex porous media.[39] According to theoretical analysis of NMR, pore radius (r) and the transverse relaxation time T_2 exhibit a linear relationship[40]

$$\frac{1}{T_2} = \rho\frac{S}{V} = F_s\frac{\rho}{r} \tag{22}$$

where ρ is the transverse surface relaxation strength of rocks, S and V are the pore surface area and volume, and F_s is the geometry factor. For

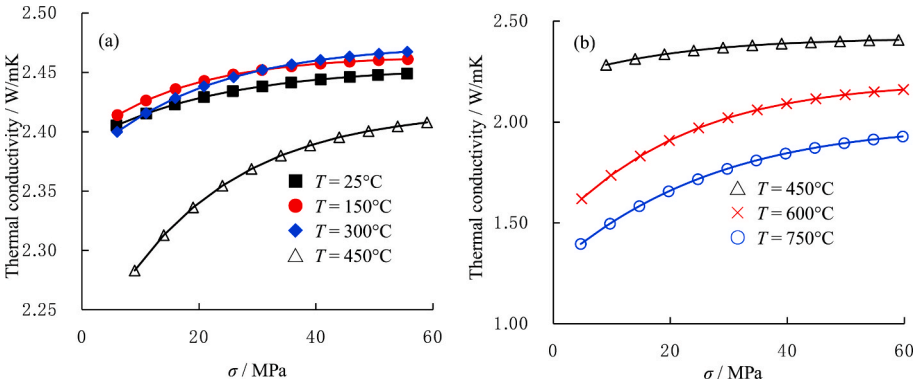

Fig. 16. Thermal conductivity following thermal treatment under varied effective stress: (a) $T \leq 450$ °C, (b) $T \geq 450$ °C.

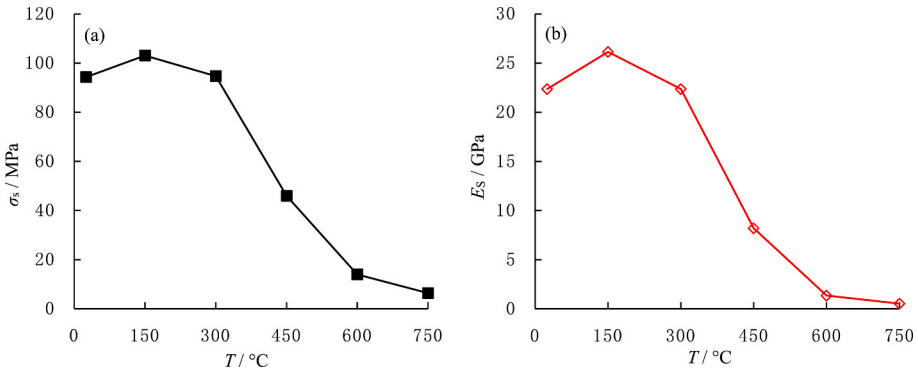

Fig. 17. Variation of peak strength and elastic modulus of granite specimens under uniaxial compression with temperature: (a) σ_s, (b) E_S.

spherical pores, $F_s = 3$, and for a columnar pipe, $F_s = 2$.

Fig. 18 illustrates the T_2 relaxation times of heat-treated granite. The amplitudes have two obvious peaks, and temperature has a significant effect on the T_2 relaxation time. The first peak (P_1) corresponds to the micropores, and the second peak (P_2) corresponds to microcracks. When $T \leq 300$ °C, temperature has only a slight effect on T_2, the area of P_1 is larger than P_2. This means that temperature has only a slight effect on the distribution of micropores and cracks, and that the micropores dominate in the specimen. When $T = 450$ °C, the area of P_1 and P_2 both increases, and the area of P_2 increases more obviously than P_1. This means that the micropore and microcrack densities increase concurrently, but that the microcrack density increases rapidly. When $T \geq 600$ °C, due to phase transformation of quartz, the areas of P_1 and P_2 increases markedly, representing that the density of the micropores and microcracks increases significantly with the microcrack dominating the porosity in the specimen.

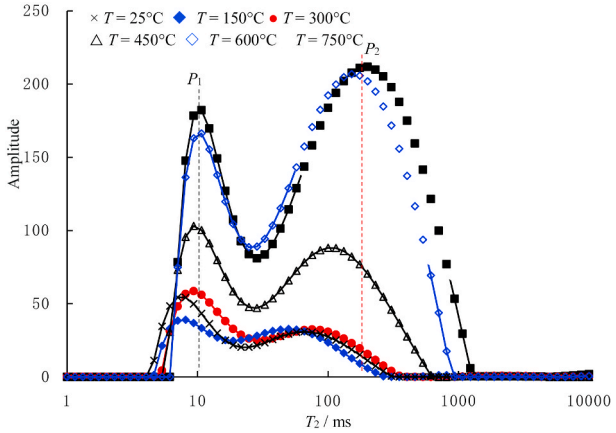

Fig. 18. T_2 NMR relaxation time following thermal treatment.

To quantitatively investigate the evolution of micropores and microcracks in the specimens following thermal treatment, the reach time of the peak and T_2 spectral area are presented in Fig. 19. The reach time of the peak and the T_2 spectral area reflect the size and density of the micropores and microcracks to some extent. As shown in Fig. 19a, the P_1 reach time remains near constant with increasing temperature, suggesting that high temperature has only a small effect on the size of the micropores. The P_2 reach time first decreases at $T = 150$ °C. From Fig. 8d, the fraction of connectivity of microcracks slightly decreases when $T = 150$ °C. When individual microcracks connect with each other, they present as a single microcrack in the NMR imaging. As a result of this, as the fraction of connectedness decreases, the average size of the microcracks slightly decreases when $T = 150$ °C. Since the fraction of connectedness decreases, the extent of the distribution of microcracks also decreases. This phenomenon is also apparent in Fig. 18 as the time between the initial and end portions of the P_2 signal decreases. At $T \geq 150$ °C, the reach time of the peak rises with increasing temperature, which suggests an increase in the size of the microcracks. It can be seen from Figs. 7 and 8d that the average half-aperture and fraction of connectedness increase with increasing temperature, resulting in an increase in the crack size.

Fig. 19b shows the variation of T_2 spectral area of P_1 and P_2 with treatment temperature. The T_2 spectral area of P_1 and P_2 remain near constant with increasing temperature, and the value of P_1 and P_2 are almost equal when $T \leq 300$ °C. This means that temperature has only a slight effect on the density of the micropores and microcracks and that the density of the micropores and microcracks are almost equal. When 300 °C $\leq T \leq 600$ °C, the T_2 spectral area of P_1 and P_2 quickly increase, and the rise rate of P_2 is larger than that of P_1. This means that high temperature generates more micropores and microcracks, although this is more obvious for the evolution of microcracks. From Figs. 7 and 8c-d,

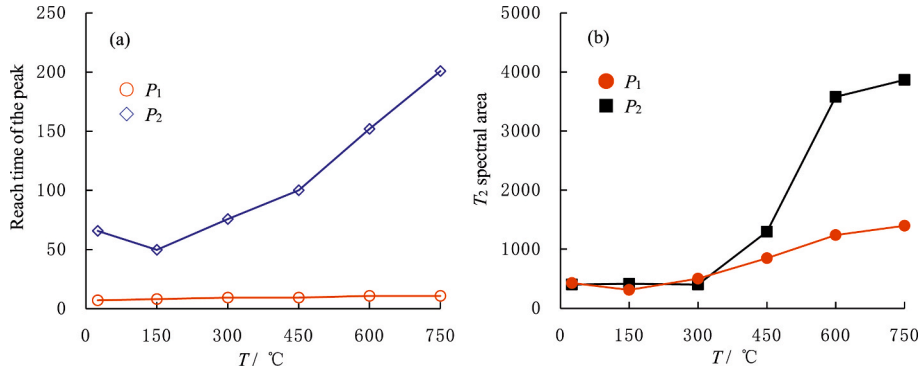

Fig. 19. Variation of the reach time to peak and T_2 spectral area with temperature: (a) reach time to peak, (b) T_2 spectral area.

although the density increase is not obvious when $T = 450$ °C, the microcrack aperture and fraction of connectedness increases significantly as apparent in the rapid increase in the T_2 spectral area. When $T = 600$ °C, microcrack aperture, microcrack density and fraction of connectedness all increase rapidly, as apparent in the rapid increase in the T_2 spectral area. At $T = 750$ °C, the T_2 spectral area rise rates of P_1 and P_2 decrease simultaneously, suggesting that the micropores and microcracks are propagating only slowly. From Figs. 7 and 8c-d, the microcrack aperture decreases slightly, and the rate of increase of microcrack density and fraction of connectivity slightly decrease. From the above analysis it can be concluded that the results recovered from the NMR imaging agree satisfactorily with the results recovered from the theoretical analysis.

It should be noted that the half aperture is larger than the radius of the microcrack, this may be due to the hypothesis in this research is not perfect, and it should be solved in future.

7. Conclusions

We investigate the evolution of microcrack aperture, density and radius with temperature and effective stress to link permeability evolution under different effective stresses for granites that develop differing porosities and formation factors following thermal treatment. The following conclusion are obtained:

(1) Initial, residual permeability and porosity are only slight affected by temperature when $T \leq 300$ °C but increase rapidly as temperature increases from 300 °C to 600 °C before finally entering a stable phase when 600 °C $\leq T \leq$ 750 °C. The formation factor first slightly decreases when temperature increases to 150 °C, then decreases rapidly when temperature increases from 150 °C to 600 °C before reaching a plateau when $T = 750$ °C.

(2) When $T = 150$ °C, microcrack aperture and radius increases, whereas microcrack density and fraction of connectedness decrease, prompting porosity, peak strength and elastic modulus to increase. When $T = 300$ °C, microcrack density decrease, whereas microcrack aperture, radius and fraction of connectedness increase, which prompts porosity to increase with peak strength and with elastic modulus remaining near constant. When $T = 450$ °C, microcrack aperture, radius and fraction of connectedness increase, which lead to an increase in porosity while peak strength and elastic modulus both decrease. When $T = 600$ °C, the phase transformation of quartz is speculated to results in microcrack aperture, radius, density and fraction of connectedness to increase rapidly, leading porosity to increase rapidly, and the peak strength and elastic modulus to decrease. When $T = 750$ °C, microcrack aperture, radius, density and fraction of connectedness increase only slightly, which result in little change in the porosity, peak strength and elastic modulus. The strength and elastic modulus decrease exponentially with fractional connectivity of the microcrack porosity. The initial compressibility of microcracks has a linear relationship with initial aperture, and the decline rate of microcrack compressibility first increases when temperature increases to 150 °C, and then remains near constant.

(3) The residual porosity first remains near constant when $T \leq 300$ °C, and then it rises slightly when temperature increases from 300 °C to 450 °C before increasing rapidly when temperature increases from 450 °C to 750 °C. The formation factor for the granite increases near-linearly with effective stress with the rate of increase generally decreasing with increasing temperature. Thermal conductivity dominated by porosity, and the relationship between thermal conductivity and effective stress can be reconstructed. Thermal conductivity first increases rapidly before becoming constant with increasing effective stress. With increasing temperature, the thermal conductivity decreases and becomes more sensitive to the effective stress.

These observations indicate that changes in mechanical and transport properties of granite are impacted significantly by thermal treatment and these effects must be accommodated in performance assessment.

Declaration of competing interest

The authors declare that they have no known competing financial interests or personal relationships that could have appeared to influence the work reported in this paper.

Acknowledgements

The research was supported by the Fundamental Research Funds for the Central Universities (2020ZDPYMS34). The authors express sincere gratitude to the editor and the anonymous reviewers for their valuable comments, which have greatly improved this paper.

References

1 Yang SQ, Ranjith PG, Jing HW, et al. An experimental investigation on thermal damage and failure mechanical behavior of granite after exposure to different high temperature treatments[J]. *Geothermics*. 2017;65:180–197.
2 Zhao XG, Cai M, Wang J, et al. Strength comparison between cylindrical and prism specimens of Beishan granite under uniaxial compression[J]. *Int J Rock Mech Min Sci*. 2015;(76):10–17.
3 Yang SQ, Huang YH, Tian WL, Yin PF, Jing HW. Effect of high temperature on deformation failure behavior of granite specimen containing a single fissure under uniaxial compression [J]. *Rock Mech Rock Eng*. 2019;52:2087–2107.
4 Yang SQ, Tian WL, Elsworth D, Wang JG, Fan LF. An experimental study of effect of high temperature on the permeability evolution and failure response of granite under triaxial compression [J]. *Rock Mech Rock Eng*. 2020. https://doi.org/10.1007/s00603-019-01982-7.
5 Gibb FGF. A new scheme for the very deep geological disposal of high-level radioactive waste[J]. *J Geol Soc*. 2000;157(1):27–36.

6 Ghabezloo S, Sulem J, Guédon S, et al. Effective stress law for the permeability of a limestone[J]. *Int J Rock Mech Min Sci*. 2009;46(2):297–306.
7 Chen D, Pan Z, Ye Z, et al. A unified permeability and effective stress relationship for porous and fractured reservoir rocks[J]. *J Nat Gas Sci Eng*. 2016;29:401–412.
8 Li Y, Tang D, Xu H, et al. Experimental research on coal permeability: the roles of effective stress and gas slippage[J]. *J Nat Gas Sci Eng*. 2014;21:481–488.
9 Chen Z, Pan Z, Liu J, et al. Effect of the effective stress coefficient and sorption-induced strain on the evolution of coal permeability: experimental observations[J]. *Int J Greenh Gas Contr*. 2011;5(5):1284–1293.
10 Bernabe Y. The effective pressure law for permeability in Chelmsford granite and Barre granite. *Int J Rock Mech Min Sci Geomech Abstr*. 1986;23(3):267–275. Pergamon.
11 McKee CR, Bumb AC, Koenig RA. Stress-dependent permeability and porosity of coal and other geologic formations[J]. *SPE Form Eval*. 1988;3(1):81–91.
12 Géraud Y. Variations of connected porosity and inferred permeability in a thermally cracked granite[J]. *Geophys Res Lett*. 1994;21(11):979–982.
13 Morrow C, Lockner D, Moore D, et al. Permeability of granite in a temperature gradient[J]. *J Geophys Res: Solid Earth*. 1981;86(B4):3002–3008.
14 Fischer GJ, Paterson MS. *Measurement of Permeability and Storage Capacity in Rocks during Deformation at High Temperature and pressure[M]//International Geophysics*. vol. 51. Academic Press; 1992:213–252.
15 Zharikov AV, Vitovtova VM, Shmonov VM, et al. Permeability of the rocks from the Kola superdeep borehole at high temperature and pressure: implication to fluid dynamics in the continental crust[J]. *Tectonophysics*. 2003;370(1-4):177–191.
16 Yasuhara H, Kinoshita N, Ohfuji H, et al. Temporal alteration of fracture permeability in granite under hydrothermal conditions and its interpretation by coupled chemo-mechanical model[J]. *Appl Geochem*. 2011;26(12):2074–2088.
17 Tanikawa W, Tadai O, Mukoyoshi H. Permeability changes in simulated granite faults during and after frictional sliding[J]. *Geofluids*. 2014;14(4):481–494.
18 Zhao Y, Feng Z, Zhao Y, et al. Experimental investigation on thermal cracking, permeability under HTHP and application for geothermal mining of HDR[J]. *Energy*. 2017;132:305–314.
19 Chen S, Yang C, Wang G. Evolution of thermal damage and permeability of Beishan granite[J]. *Appl Therm Eng*. 2017;110:1533–1542.
20 Jiang G, Zuo J, Ma T, et al. *Experimental Investigation of Wave Velocity-Permeability Model for Granite Subjected to Different Temperature Processing[J]*. vol. 2017. Geofluids; 2017.
21 Davies JP, Davies DK. *Stress-dependent Permeability: Characterization and modeling [C]//SPE Annual Technical Conference and Exhibition*. Society of Petroleum Engineers; 1999.
22 Klinkenberg LJ. *The Permeability of Porous Media to Liquids and gases[C]//Drilling and Production Practice*. American Petroleum Institute; 1941.
23 The permeability of porous media to liquids and gaseScheidegger A. *The Physics of Flow through Porous Media*. London: University Of Toronto Press; 1958.
24 Archie GE. The electrical resistivity log as an aid in determining some reservoir characteristics[J]. *Trans AIME*. 1942;146(1):54–62.
25 Dienes JK. *Permeability, Percolation and Statistical Crack mechanics[C]//The 23rd US Symposium on Rock Mechanics (USRMS)*. American Rock Mechanics Association; 1982.
26 Gueguen Y, Dienes J. Transport properties of rocks from statistics and percolation[J]. *Math Geol*. 1989;21(1):1–13.
27 Stauffer D, Aharony A. *Introduction to Percolation theory[M]*. Taylor & Francis; 2018.
28 Davies JP, Davies DK. *Stress-dependent Permeability: Characterization and modeling [C]//SPE Annual Technical Conference and Exhibition*. Society of Petroleum Engineers; 1999.
29 Sundberg J, Hellström G. Inverse modelling of thermal conductivity from temperature measurements at the Prototype Repository, Äspö HRL[J]. *Int J Rock Mech Min Sci*. 2009;46(6):1029–1041.
30 Zhao XG, Wang J, Chen F, et al. Experimental investigations on the thermal conductivity characteristics of Beishan granitic rocks for China's HLW disposal[J]. *Tectonophysics*. 2016;683:124–137.
31 Mousset-Jones P, McPherson MJ. The determination ofin situ rock thermal properties and the simulation of climate in an underground mine[J]. *Int J Min Geol Eng*. 1986;4(3):197–216.
32 Innaurato N, Occella E. *Laboratory and in Situ Rock Thermal Property Measurements in Hot mine[C]//ISRM International Symposium*. International Society for Rock Mechanics and Rock Engineering; 1989.
33 Görgülü K, Durutürk YS, Demirci A, et al. Influences of uniaxial stress and moisture content on the thermal conductivity of rocks[J]. *Int J Rock Mech Min Sci*. 2008;45(8):1439–1445.
34 Demirci A, Görgülü K, Durutürk YS. Thermal conductivity of rocks and its variation with uniaxial and triaxial stress[J]. *Int J Rock Mech Min Sci*. 2004;41(7):1133–1138.
35 Huang YH, Yang SQ, Tian WL, et al. Physical and mechanical behavior of granite containing pre-existing holes after high temperature treatment[J]. *Arch Civ Mech Eng*. 2017;17(4):912–925.
36 Sun Q, Zhang W, Xue L, et al. Thermal damage pattern and thresholds of granite. *Environ Earth Sci*. 2015;74(3):2341–2349.
37 Mitchell EK, Fialko Y, Brown KM. Temperature dependence of frictional healing of Westerly granite: experimental observations and numerical simulations[J]. *G-cubed*. 2013;14(3):567–582.
38 Tang Z C , Zhang Q Z , Peng J . Effect of thermal treatment on the basic friction angle of rock joint[J]. Rock Mech Rock Eng, doi.org/10.1007/s00603-019-02026-w.
39 Yao Y, Liu D, Che Y, et al. Petrophysical characterization of coals by low-field nuclear magnetic resonance (NMR)[J]. *Fuel*. 2010;89(7):1371–1380.
40 Chen S, Tang D, Tao S, et al. Fractal analysis of the dynamic variation in pore-fracture systems under the action of stress using a low-field NMR relaxation method: an experimental study of coals from western Guizhou in China[J]. *J Petrol Sci Eng*. 2019;173:617–629.